Tsunami wave characteristics in Sendai Bay, Japan, following the 2016 Mw 6.9 Fukushima earthquake

An-Chi Cheng [a],[*], Anawat Suppasri [a],[b], Mohammad Heidarzadeh [c], Bruno Adriano [a],[b], Constance Ting Chua [b], Fumihiko Imamura [a],[b]

[a] *Civil and Environmental Engineering, Graduate School of Engineering, Tohoku University, 6-6-06 Aoba, Aramaki-Aza, Aoba, Sendai, 980-0845, Japan*
[b] *International Research Institute of Disaster Science, Tohoku University, 468-1 Aoba, Aramaki-Aza, Aoba, Sendai, 980-0845, Japan*
[c] *Department of Architecture and Civil Engineering, University of Bath, BA2 7AY, UK*

A B S T R A C T

On 21 November 2016, a Mw 6.9 intraplate earthquake occurred off the Fukushima coast in Japan, triggering a moderate-size tsunami with amplifications and long oscillations along the Sendai Bay coast. Here, we apply a hybrid approach to hindcast the wave characteristics in the Sendai Bay during the 2016 tsunami event, by analyzing coastal tide records, spectral analyses, and tsunami simulations. Our analysis shows that tsunami wave on tide stations mainly carried wave periods of 3.8–22.5 min, triggered by source periods of 18.5–22.5 min. The long oscillation in Sendai Bay was due to longer period of >28.8 min, affected by the presence of edge waves and oscillation of Sendai Bay. High-energy wave was found to be significant in most oscillation periods inside the Sendai Bay and around the Oshika Peninsula. The spatial distribution of maximum spectral and simulated tsunami amplitudes also reveal that the radiated tsunami energy was entrapped in the nearshore areas, resulting in resonance amplifications in the Sendai Bay.

1. Introduction

On 21 November 2016, a large normal-faulting intraplate earthquake occurred off Fukushima coast, Japan at 20:59:47 UTC (Japan Standard Time- JST - of 11:59:47). The Japan Meteorological Agency (JMA) located the earthquake epicenter being at 37.355 °N and 141.604 °E at a depth of 25 km with a JMA magnitude (M_{jma}) of 7.4. The moment tensor solution was estimated by several agencies, such as the United States Geological Survey (USGS), Global CMT Catalog Project, and the National Research Institute of Earth Science and Disaster Resilience (NIED). The USGS suggested a moment magnitude (M_w) of 6.9 at a depth of 9.0 km; GCMT reported an M_w of 6.9 at a depth of 12.0 km; and NEID calculated a moment magnitude of 7.0 at a depth of 11.0 km.

The earthquake triggered a moderate-size tsunami, which attacked the northern Pacific coast of Japan. Signals of the tsunami were recorded at several coastal tide gauges along northern Pacific coast of Japan. Fig. 1 shows the map of tsunami warnings (red) and advisories (yellow) issued by the JMA during the 2016 Fukushima tsunami. At 21:02 UTC (approximately 2 min after the earthquake), the JMA issued an initial tsunami warning stating possible tsunami height of up to 3 m for the

Fukushima Prefecture, and a lower level of tsunami advisory (i.e., possible tsunami height of up to 1 m) for other coastal regions along northern Pacific coast of Japan, including Aomori, Iwate, Miyagi, Ibaraki, and Chiba Prefectures (Fig. 1) (Suppasri et al., 2017). However, 2 h later at 23:09 UTC, JMA upgraded the warning level of Miyagi Prefecture from "advisory" to "warning", due to the unexpected arrival of higher tsunami waves. At 03:50 UTC, JMA cancelled the tsunami warning advisory of all regions along northern Pacific coast of Japan. The maximum zero-to-crest tsunami amplitude recorded at the Sendai Port was 1.4 m – the highest recorded in Miyagi Prefecture since the giant March 2011 Tohoku-oki tsunami. One of the important phenomena that was observed during this event was the delayed local amplification of tsunami wave (2 h after the earthquake origin time) and its long-lasting duration in Sendai Bay. This long tsunami oscillations were not observed in other locations along the Fukushima coast during this event.

A number of studies have attempted to reproduce the 2016 Fukushima earthquake and tsunami through numerical simulations. For instance, a preliminary study by Suppasri et al. (2017) modelled the 2016 Fukushima tsunami by using nonlinear shallow water equations

and applying the single fault model proposed by USGS (2016). Suppasri et al. (2017) noted the presence of amplified waves in the Sendai Bay and suggested possible causes for them such as wave shoaling and refraction inside the bay. Gusman et al. (2017) and Adriano et al. (2018) conducted tsunami inversion analyses using available tsunami waveform data to obtain the fault slip distribution. They showed that the heterogeneous slip models can exhibit better performance in reproducing tsunami observations. Gusman et al. (2017) also tested the sensitivity of tsunami wave heights to earthquake parameters such as fault size and depth, demonstrating that a single fault with dimensions of 20 km × 10 km and a fault depth of 12 km can reproduce tsunami waveforms with good agreements to the observations. In another study, Kuramoto et al. (2018) performed multiple scenario simulations to evaluate the relationship between the earthquake parameters and the tsunami heights measured at the Sendai Port. Kuramoto et al. (2018) concluded that the fault strike of the 2016 Fukushima earthquake differed from that assumed for the area by the JMA during their tsunami warning operations, resulting in the underestimation of tsunami heights at the Sendai Port. More recently, Hayashi (2021) quantified the impacts of fault strike on the distribution of simulated tsunami heights along the north Pacific coast of Japan and found that tsunami height distribution along the Sanriku coast (i.e., a coastline with incised valleys) depends on the source directivity and wave reflections.

In summary, we note that the above studies were mostly focused on the influence of source models and fault parameters on tsunami genesis in the Fukushima region, with little consideration of other important factors that might influence wave characteristics observed during the 2016 event. Additionally, while some of these studies acknowledged the presence of local wave amplifications in the Sendai Bay, the mechanisms behind the amplification have not been investigated. Considering these research gaps in the literature, the objective of this research is twofold: (1) to understand the feature of tsunami waveform measured at coastal tide stations; and (2) to explain why tsunami was amplified inside of Sendai Bay and around the Oshika Peninsula.

Here, firstly, waveform analysis was applied to tsunami observations at coastal tide gauges along the northern Pacific coast of Japan. Following this, tsunami simulation was conducted, and simulations were compared with the actual tsunami observations. Finally, spectral analyses (Fourier and Wavelet analyses) were applied to the tsunami observations and simulated tsunami wavefields, respectively, to assess the wave characteristics and amplification mechanisms inside the Sendai Bay. This study presents the first attempt to evaluate the wave characteristics and amplification mechanisms of the 2016 Fukushima earthquake and tsunami. This paper also demonstrates the source dimension properties of the 2016 Fukushima earthquake from tsunami perspectives. The findings of this study can be beneficial for tsunami warning operations and coastal emergency management along the north Pacific coast of Japan and worldwide.

2. Data and methods

2.1. Tsunami waveforms

Tide gauges record sea level variations, and the time series of these tidal records allow us to capture local and regional phenomena such as tides, tsunami, storm surges and other coastal processes. To understand tsunami wave characteristics and behavior of the 2016 event, we collected and processed tide records from five coastal tide gauges along the north Pacific coast of Japan, namely Ofunato, Ayukawa, Sendai Port, Soma, and Onahama for our analyses (Fig. 2). These tide gauges are operated and maintained by the JMA. Since the 2016 Fukushima earthquake occurred at 20:59:49 UTC, we used tide records from 00:00:00 UTC on 21 November 2016 until 00:00:00 UTC on 26 November 2016. All tide records have a sampling interval of 15 s and include ocean tide. The ocean tide components were filtered out from the original tide records by applying a high pass filter with a cutoff frequency of 0.00006944 Hz (14400 s). This method has been applied by several authors to produce tsunami waveforms (e.g., Heidarzadeh et al., 2021; Wang et al., 2022a; Cheng et al., 2023a); this approach gives similar results to the one based on removing calculated ocean tides from the raw tide records as reported by Heidarzadeh et al. (2015). The original tide records and tsunami waveforms at coastal tide gauges are plotted in Figs. 3 and 4, respectively.

2.2. Tsunami simulation

Tsunami waveforms recorded at tide stations represent wave characteristics in a single point in space over time, i.e., at the location of the
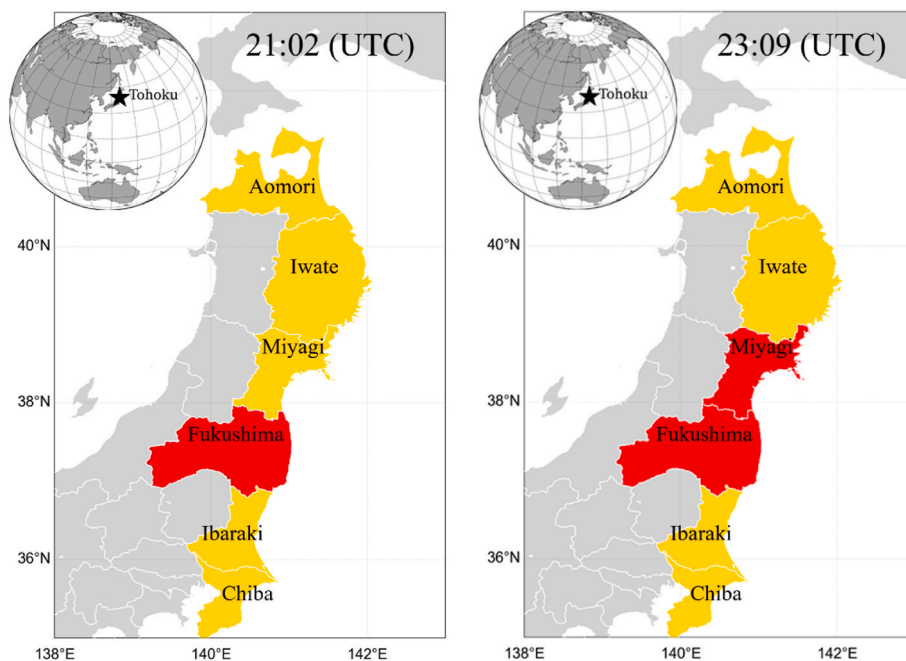

Fig. 1. Tsunami warnings (red) and advisories (yellow) issued by the Japan Meteorological Agency (JMA) during the 2016 Fukushima tsunami (JMA, 2016).
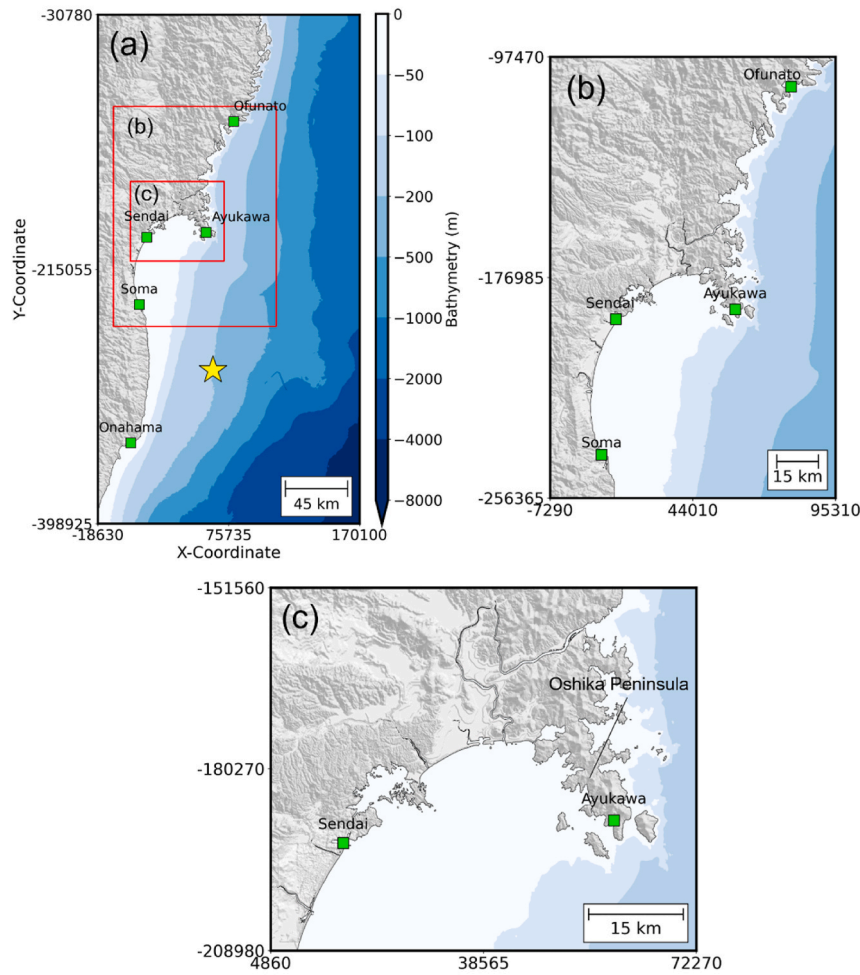
Fig. 2. Topography and bathymetry of the grids of (a) region 1 (spatial resolution = 405 m), (b) region 2 (spatial resolution = 135 m), and (3) region 3 (spatial resolution = 45 m) for tsunami numerical simulations. The yellow star represents the epicenter of the 2016 Fukushima earthquake. The green squares denote the locations of coastal tide stations, and the red rectangles frame the computational regions 2 and region 3 within region 1.

tide gauge. Tsunami simulation can supplement tide gauge data by adding a spatial dimension, allowing us to interpret the wave characteristics across space and time. We performed numerical simulation to study the tsunami waveforms and propagation paths of the 2016 Fukushima tsunami around the Sendai Bay. To set up the initial conditions for our simulation, we employed the earthquake slip distributions proposed by Gusman et al. (2017) and Adriano et al. (2018). The rationale for considering two independent slip models was to test the sensitivity of tsunami simulations to different source models. These two independent source models (Table 1) were derived through the inversion of observed tsunami waveforms and are therefore expected to produce better performances than uniform slip models (Wang et al., 2021). Detailed information of the source models employed for tsunami numerical simulations is listed in Table 1. For example, the maximum slip values reported by Gusman et al. (2017) and Adriano et al. (2018) are 3.4 m and 4.7 m, respectively.

For each earthquake slip model, initial vertical seafloor displacement was calculated using the Okada's theory (Okada, 1985). In addition, since the horizontal motion on sea slopes has sometimes important impacts on tsunami generation, here, the initial horizontal seafloor displacement was calculated following the method introduced by Tanioka and Satake (1996). The initial seafloor displacement of each earthquake slip model is shown in Fig. 5. The numerical package TUNAMI-N2 was used to simulate tsunami propagation from the source region to the Sendai Bay. TUNAMI-N2 was developed at Tohoku

University (Japan) to simulate the wave propagation of near-field tsunamis based on nonlinear theory of the shallow water equations, which is solved using a leap-frog scheme in Finite Difference Method (Goto et al., 1997; Imamura, 1996). The continuity and nonlinear shallow water equations solved by TUNAMI-N2 are presented in the following:

$$\frac{\partial \eta}{\partial t} + \frac{\partial M}{\partial x} + \frac{\partial N}{\partial y} = 0 \tag{1}$$

$$\frac{\partial M}{\partial t} + \frac{\partial}{\partial \chi}\left(\frac{M^2}{D}\right) + \frac{\partial}{\partial y}\left(\frac{MN}{D}\right) + gD\frac{\partial \eta}{\partial \chi} + \frac{gn^2}{D^{\frac{7}{3}}}M\sqrt{M^2+N^2} = 0 \tag{2}$$

$$\frac{\partial N}{\partial t} + \frac{\partial}{\partial \chi}\left(\frac{MN}{D}\right) + \frac{\partial}{\partial y}\left(\frac{N^2}{D}\right) + gD\frac{\partial \eta}{\partial y} + \frac{gn^2}{D^{\frac{7}{3}}}N\sqrt{M^2+N^2} = 0 \tag{3}$$

where M and N are the discharge fluxes in the x and y directions, respectively, η is the water level, g is the gravitational acceleration (9.81 m s^{-1}), D is the total water depth, and n is Manning's roughness coefficient. The Manning's roughness coefficient was set to a uniform value of 0.025 s m$^{-1/3}$ for all computational grids, which is often used for seafloor's roughness (Japan Society of Civil Engineers (JSCE), 2016; Adriano et al., 2018; Suppasri et al., 2022).

To save the computational time, the tsunami propagation simulation was conducted on a three-level nested grid system following a 1/3 ratio rule (the ratio between the grid sizes of the parent and child grids) (i.e.,
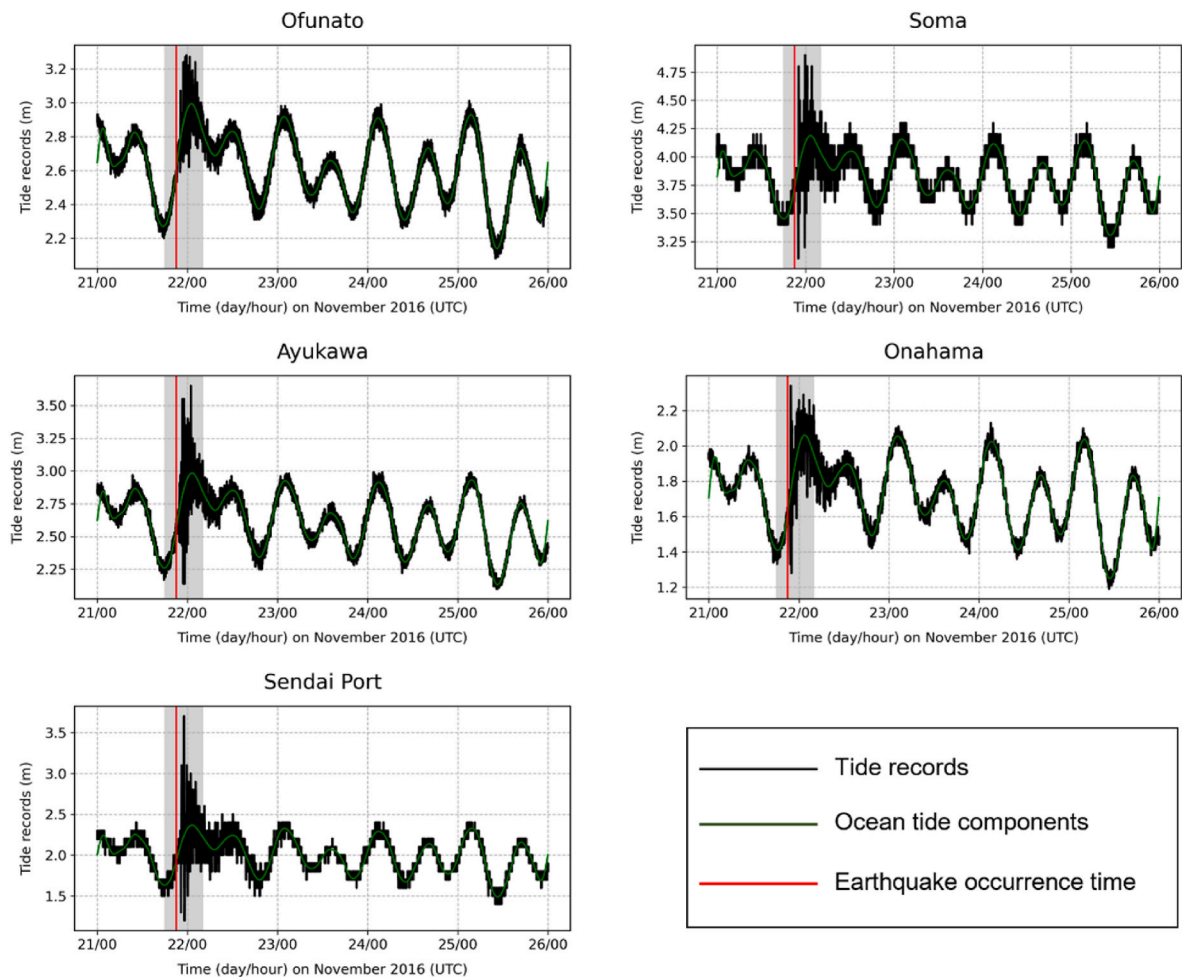
Fig. 3. Tide gauge records along East Japan coast during the 2016 Fukushima tsunami. The solid red lines denote Earthquake Occurrence Time (EOT). The solid green lines indicate the ocean tide signals. The gray areas show the time segments of the primary tsunami signals.

grids with sizes of 405 m, 135 m, and 45 m as shown in Fig. 2). The topographic and bathymetric data employed for tsunami numerical simulation was obtained from a previous study (Suppasri et al., 2022), which used the original data provided by Geospatial Information Authority of Japan (GSI) (https://www.gsi.go.jp/kankyochiri/Laser_demi mage.html). The coarsest grid region of 405 m covers the geographical region of the East Japan, whereas the finer grid regions of 135 m and 45 m cover coastal areas around the Sendai Bay and the Oshika Peninsula. The inundation computation was not included in the tsunami simulation as no tsunami flooding was reported during the 2016 Fukushima tsunami; thus, the reflective boundary condition was applied along the shorelines. The computation time step in the nested grid system was set to 0.1 s to satisfy the stability condition of the numerical simulations. We simulated the 2016 Fukushima tsunami activity with a total elapsed time of 12 h. The maps of topographic and bathymetric data adopted for tsunami simulations are shown in Fig. 2.

2.3. Spectral analysis

Tsunami waveforms from both tide gauges and our numerical simulations underwent spectral analyses. Spectral analysis is a technique to decompose time series into periodic components, and the spectra illustrates the energetic peaks across various frequency bands. In this study, our spectral analyses comprise of waveform spectral analyses (time series in a single location) and spatio-temporal spectral analyses (time series in the spatial domain).

For waveform spectral analyses, two types of analyses were

performed: Fourier and Wavelet (time-frequency) analyses. Spectra at each tide gauge station was estimated using the Fourier-Welch method, and we applied Hanning's (Hann) window with 50% overlaps to reduce spectral leakage (e.g., Heidarzadeh et al., 2017; Heidarzadeh and Gusman, 2021). Spectra analysis (i.e., Fourier-Welch analysis) was set for 12 h before and after the tsunami arrival (24 h in total), which means time series between 10:00:00 UTC on 21 November 2016 and 10:00:00 UTC on 22 November 2016. Inspection of background signals gave no indications of any storm or other oceanic events that could influence our analyses. Next, Wavelet analysis was conducted to the de-tided waveforms to study the oscillation patterns of the tsunami and the temporal changes of the dominant spectral peaks, following the method by Torrence and Compo (1998). The time series between 18:00:00 UTC on 21 November 2016 and 18:00:00 UTC on 22 November 2016 were employed for Wavelet analysis. We applied the Morlet mother function for our Wavelet analysis as it showed satisfactory performance in previous studies (e.g., Heidarzadeh et al., 2020, 2022a; Heidarzadeh and Mulia, 2021).

To investigate whether the amplification of the 2016 Fukushima tsunami in the Sendai Bay was due to the excitation of resonance modes, we conducted tsunami resonance analysis. The analysis of tsunami resonance requires not only the spectral characteristics of tsunami wave at individual stations but also their spatial characteristics (Cortés et al., 2017; Wang et al., 2022b). However, a tide gauge station only represents a point in space and does not represent the entire wavefield. To paint a full picture of the spatio-temporal wave behavior in our region of interest, Fourier analysis was applied to the entire simulated wavefield
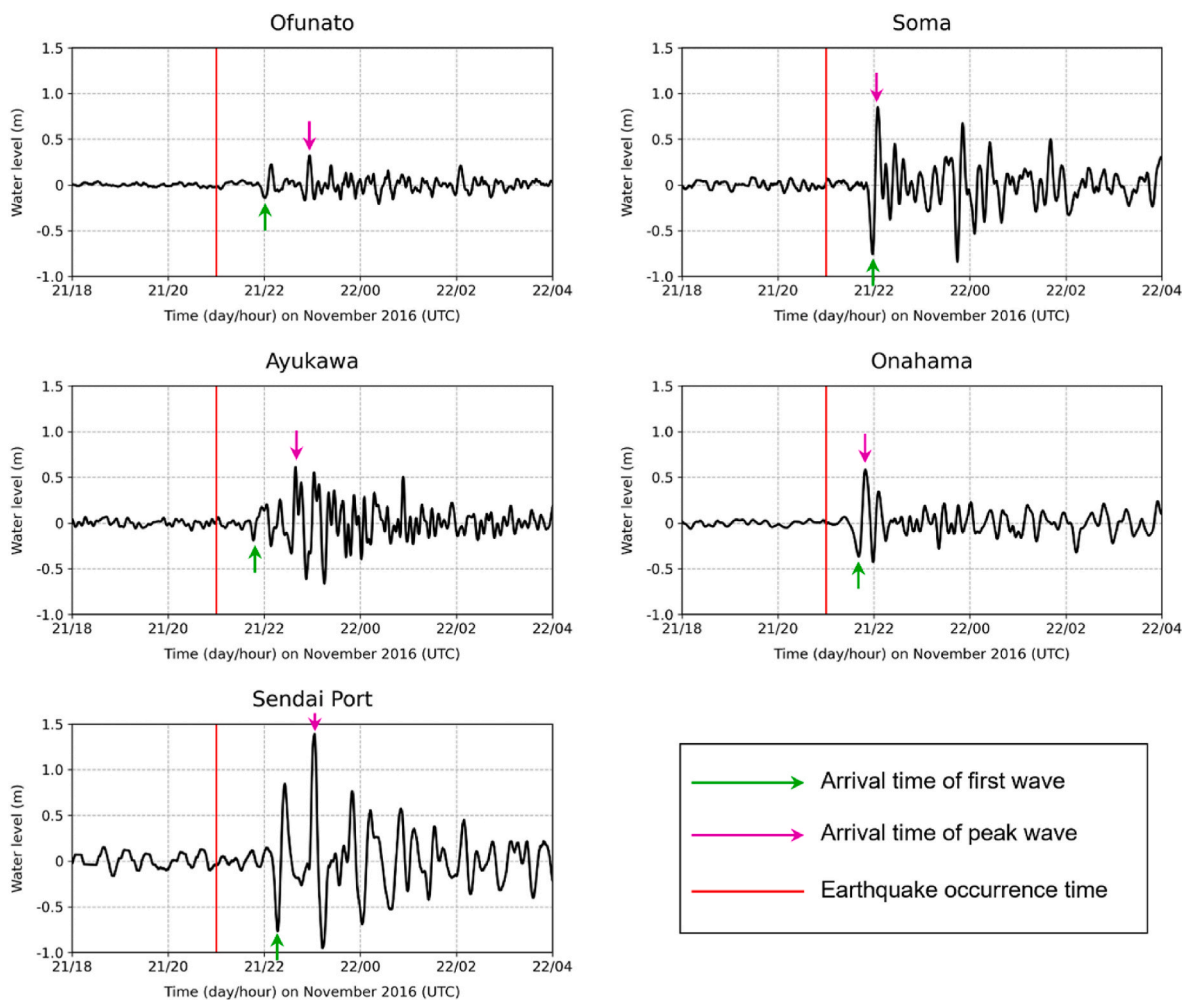
Fig. 4. Tsunami waveforms of the 2016 Fukushima earthquake at coastal tide gauges. The solid red lines indicate the Earthquake Occurrence Time (EOT). The magenta arrows denote the arrival times of the peak wave. The green arrows indicate the arrival times of the first wave troughs.

Table 1
Information of the earthquake source models employed in this study for modeling the 2016 Fukushima tsunami.

Model	Length (km)	Width (km)	Strike (deg)	Dip (deg)	Rake (deg)	Depth (km)	Slip (m)	Crustal deformation (m)
Gusman et al. (2017)	40	30	45	41	−95	1.4–14.5	0–3.4	0.08~ −1.87
Adriano et al. (2018)	40	32	49	35	−89	1.5–15.3	0–4.7	0.13~ − 1.29

corresponding to all computational grid points in the domain of region 2 (see Fig. 2b). Region 2 covers Sendai Bay and Oshika Peninsula with a spatial grid spacing of 135 m, which comprises 760 and 1177 grid points in *x* and *y* directions, respectively. In this region, the simulated time series at all grid points were outputted as time series and then were employed as inputs for Fourier analysis. To reduce the computational cost, the grid points of land, lakes, and rivers were excluded from calculations by applying a zero mask.

3. Results

3.1. Tsunami waveform features

The first tsunami wave from the 2016 Fukushima earthquake was recorded as a trough at all tide gauges in the study area (Fig. 4), as expected from a tsunami from a normal-faulting earthquake. Following the leading trough phase, the first wave crest appears at Onahama station with an amplitude of 0.58 m; at Ayukawa station with 0.19 m amplitude; at Soma station with 0.84 m amplitude; at Ofunato with 0.22 m

amplitude; and at Sendai Port with 0.84 m amplitude. At Onahama and Soma stations, the first crest was the maximum one while the maximum crest occurred later (i.e., more than 30 min after the first tsunami arrivals) in other stations. The maximum wave recorded at Ayukawa station was 0.61 m, at Ofunato was 0.32 m, and at Sendai Port was 1.38 m. At these three stations, the largest waves and persistent oscillations were recorded in the later phases. Table 2 summarizes detailed information and the physical characteristics of tsunami waveforms at each station.

3.2. Tsunami simulation and validation

The purpose of tsunami simulation is to confirm the co-seismic source of the 2016 Fukushima event and to validate it against coastal tide observations. In addition, the validated simulated waveforms at all grid points were later used for Fourier analysis in a spatial domain. Tsunami waveforms were simulated and compared with observed records at each coastal tide station. Fig. 6 shows the comparison between observed (black solid lines) and simulated tsunami waveforms given by
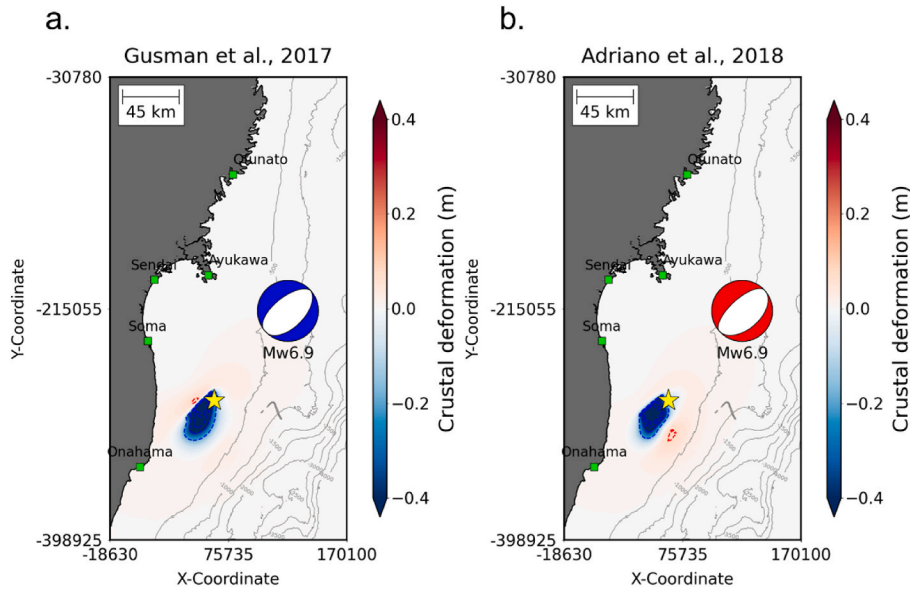
Fig. 5. The calculated crustal deformation of the 2016 Fukushima earthquake using earthquake slip models proposed by (a) Gusman et al. (2017) and (b) Adriano et al. (2018). The green squares denote the locations of tide gauge stations and yellow stars represent the epicenter. The beachballs illustrate the focal mechanisms of earthquake.

Table 2
Physical characteristics of tsunami waveforms at coastal tide gages during the 2016 Fukushima tsunami. The parameters are calculated relative to the main shock, Mw 6.9 at 20:59:49 UTC. Here we report zero-to-crest amplitudes.

Station	Longitude (° E)	Latitude (° N)	Tsunami wave amplitude (m)		
			First trough	First crest	Maximum wave crest
Ofunato	141.75	39.02	−0.14	0.22	0.32
Ayukawa	141.51	38.30	−0.19	0.19	0.61
Sendai Port	141.02	38.27	−0.76	0.84	1.38
Soma	140.96	37.83	−0.75	0.84	0.84
Onahama	140.89	36.93	−0.37	0.58	0.58

Station	Arrival time (UTC)			Visible period (min)
	First trough	First crest	Maximum wave crest	
Ofunato	22:02	22:10	22:58	15–20
Ayukawa	21:48	22:04	22:40	15–20
Sendai Port	22:18	22:27	23:05	20–40
Soma	22:00	22:05	22:05	15–20
Onahama	21:42	21:50	21:50	15–20

source models of Gusman et al. (2017) (blue solid lines) and Adriano et al. (2018) (red solid lines). Generally, tsunami simulations using both models produced good agreements between observed and simulated tsunami waveforms at all tide gauge stations, including the wave heights and arrival times of the tsunami. To evaluate the fit between observed and simulated waveforms from each source model, the misfit criterion was applied following the misfit equation by Heidarzadeh and Mulia (2022b):

$$\varepsilon = \frac{1}{N} \sqrt{\sum_{i=1}^{N} \frac{(O_i - S_i)^2}{O_i^2}} \tag{4}$$

where, ε is the misfit between observed and simulated tsunami waveforms, O_i and S_i represent the observed and simulated values, respectively, and N denotes the total data points in the times series. It should be noted that equation (4) calculates only the misfit for a particular tide

gauge station. For cases with multiple observations, the overall misfit is calculated from the average of ε for all stations. The misfits are shown at each panel in Fig. 9. The average misfit from all five tide stations is 1.33 for the source model by Gusman et al. (2017), and 1.29 for that of Adriano et al. (2018), indicating a better performance from the source model of Adriano et al. (2018).

In addition to the tsunami amplitude, simulated and observed tsunami spectra were compared at each station. In Fig. 7, the blue and red curves display the simulated tsunami spectra produced by the source models of Gusman et al. (2017) and Adriano et al. (2018), respectively. The black curves illustrate the tsunami spectra for the observations. In general, the simulated tsunami spectra from both models matched well with observations with similar shapes and peak periods. Simulated results from the numerical models were able to satisfactorily replicate the tsunami characteristics of the 2016 Fukushima event, and therefore, it is reasonable to employ the simulation results for tsunami resonance analysis in Section 3.5.

Snapshots of simulated tsunami wave propagation (i.e., using the validated source model of Adriano et al., 2018) along north Pacific coast of Japan and Sendai Bay are shown in Figs. 8 and 9. The tsunami wave propagated toward Fukushima coast after generation. The radiated tsunami waves were entrapped in nearshore areas and propagated along the coastline of Fukushima and Miyagi Prefectures as edge waves. Because of the repeated reflections and refractions along the continental edge, the alongshore oscillation was energetic and lasted remarkably long. As the waves enter the shallow waters of the Sendai Bay, a wide basin with an average sea depth of approximately 50 m, wave heights were significantly amplified as they undergo repeated incidence, shoaling and reflections and experience bay oscillations and edge waves (see Sendai Port record in Fig. 4).

3.3. Fourier spectra

Fourier spectra for tsunami (solid red lines) and background (solid black lines) signals are shown in Fig. 10 for each coastal tide station. The background spectra denote the frequency components of normal oscillations before tsunami arrival at each station. Differences in the shape and energetic peaks of the background spectra indicate that the periods of normal pre-tsunami oscillations vary from one location to another. A significant gap is seen between background and tsunami spectra in
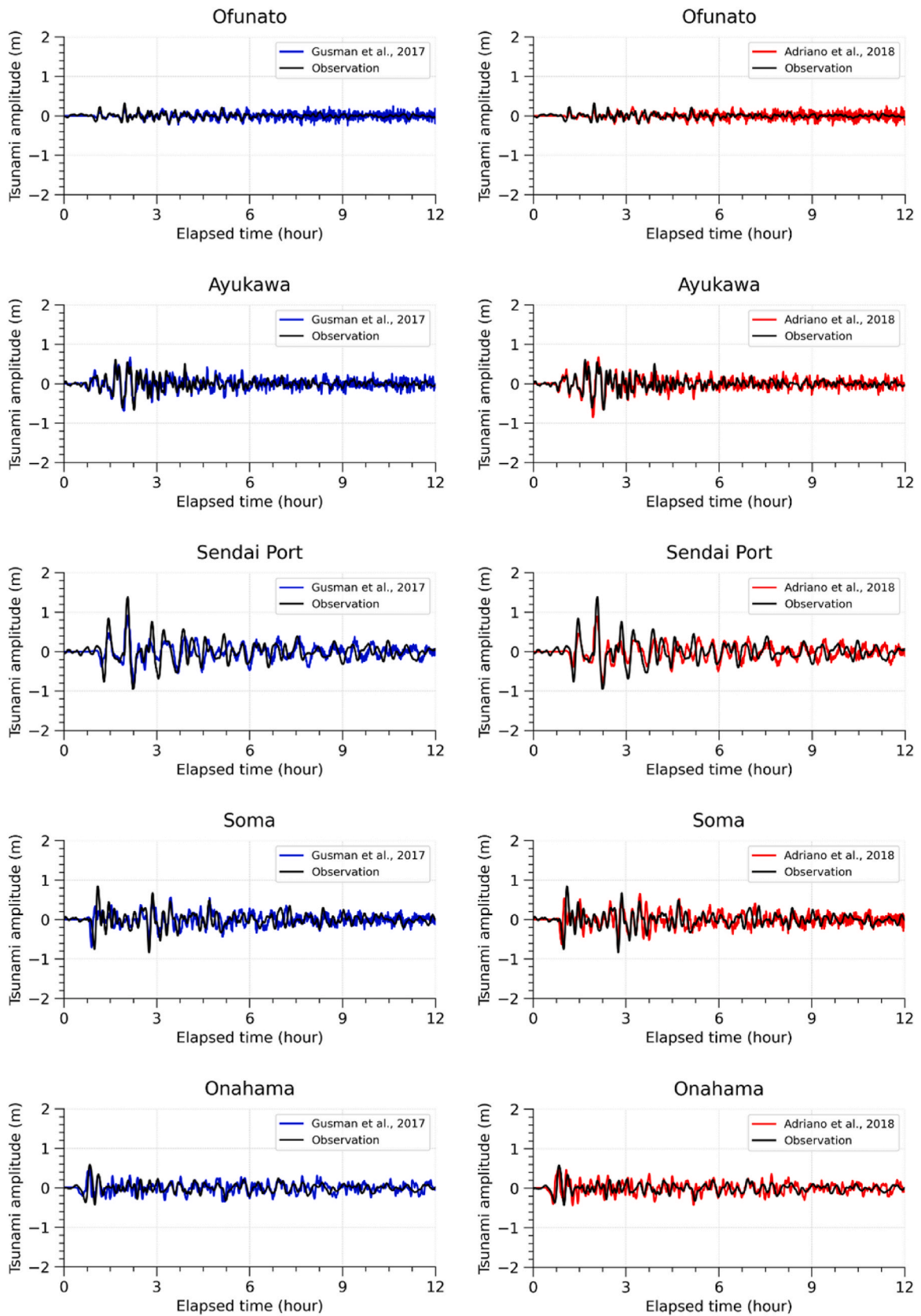
Fig. 6. Comparison of observed (black solid lines) and simulated tsunami waveforms using earthquake slip models of Gusman et al. (2017) (blue solid lines) and Adriano et al. (2018) (red solid lines).
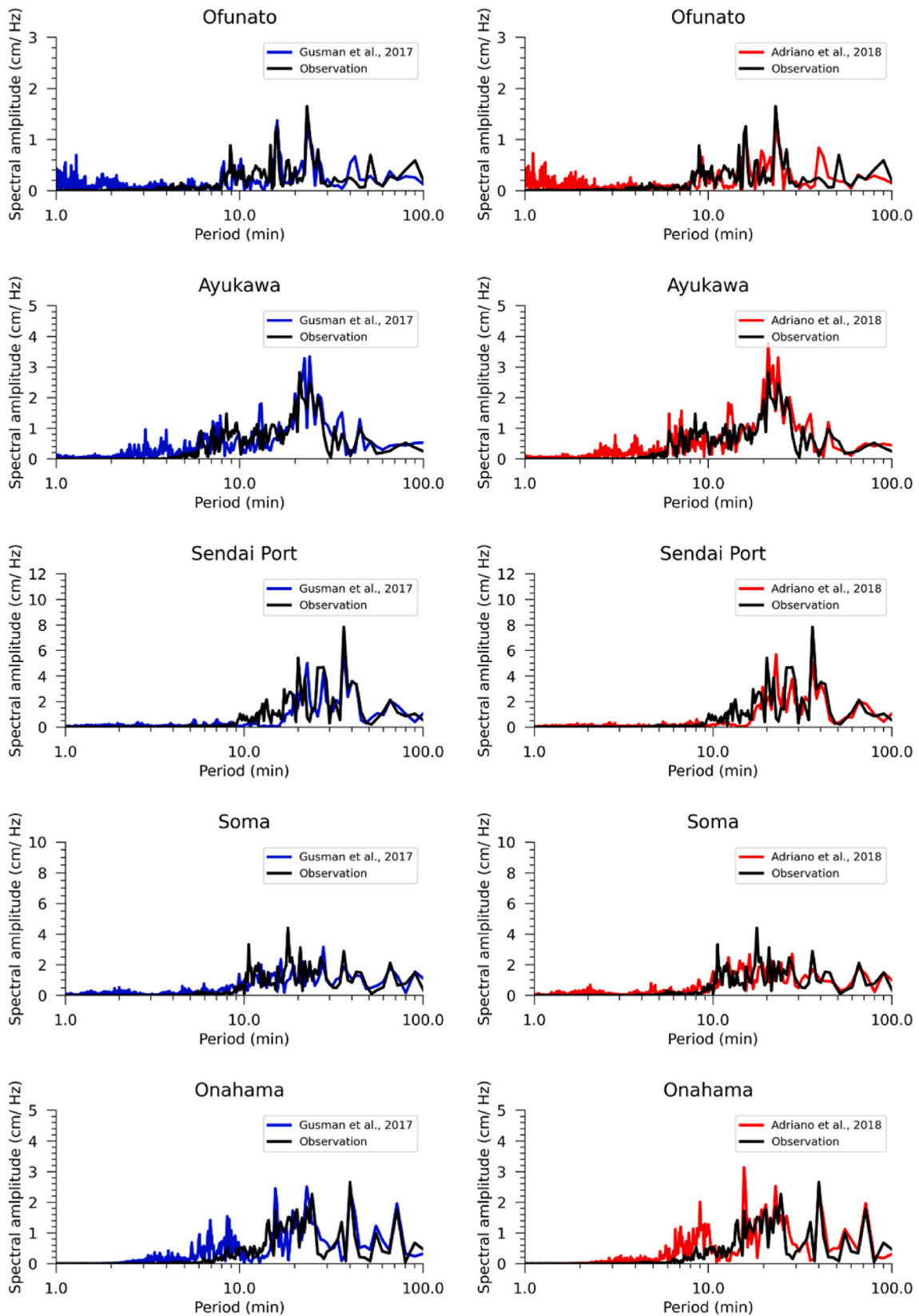
Fig. 7. Comparison of observed (black solid lines) and simulated tsunami spectra using the earthquake slip models of Gusman et al. (2017) (blue solid lines) and Adriano et al. (2018) (red solid lines).
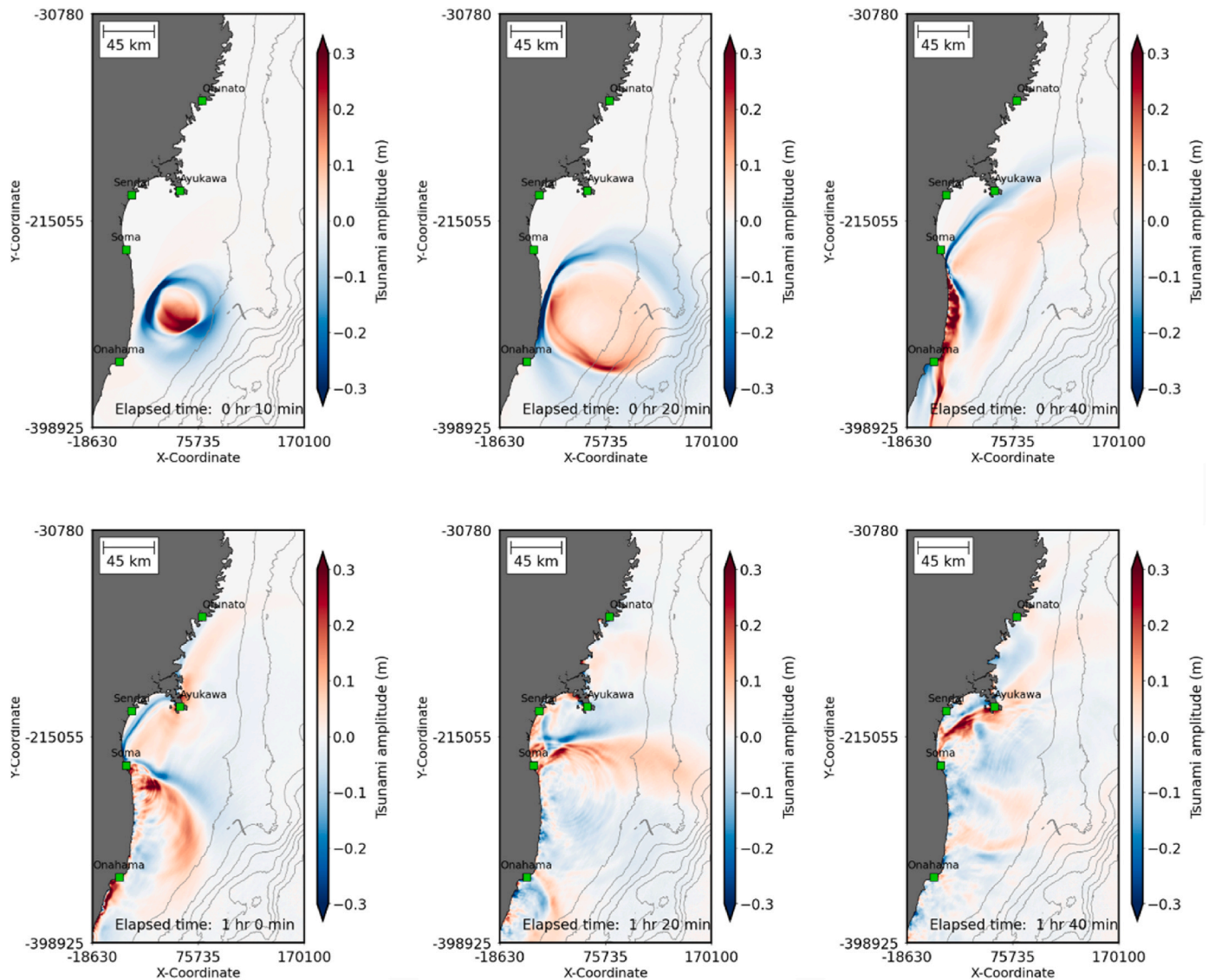
Fig. 8. Snapshots of simulated tsunami propagation along north Pacific coast of Japan following the 2016 Fukushima earthquake. The green squares denote the locations of coastal tide stations.

periods longer than 3.8 min at most stations. Tsunami spectra are helpful for identifying tsunami characteristics, such as for estimating source dimensions (Heidarzadeh and Satake, 2015; Heidarzadeh et al., 2022), propagation properties, as well as the oscillation patterns (Rabinovich, 1997; Wang et al., 2021, 2022a).

From Fig. 10, the tsunami spectra for coastal tide stations show multiple peak periods, i.e., 28.8 min, 22.5 min, 18.5 min, 11.5 min, 9.1 min, 6.5 min, 5.7 min, 4.8 min, and 3.8 min. We can identify three period bands out of these peak periods which are 18.5–22.5 min, 9.1–11.5 min, and 3.8–6.5 min. It is important to note that the Sendai port station shows oscillations at periods longer than 28.8 min which is not seen in other stations.

3.4. Wavelet spectra

Wavelet spectra of tsunami waveform reveals spectral energy bands across time (Fig. 11). The areas clustered in red and orange colors indicate higher energy levels and dominant wave periods. The first signals at each station are generally attributed to the tsunami source (Heidarzadeh et al., 2020). At all stations, energetic signals first appeared at 9.1–22.5 min after 21:30 UTC 21 November 2016,

corresponding to the arrival time of the first tsunami wave. This matched well with the Fourier spectra, suggesting that the period band of 9.1–22.5 min is likely the tsunami source periods. It is notable that wavelet and Fourier analyses possess different degrees of accuracies. Unlike Fourier spectra, the wavelet spectra account for temporal evolution and hence lose significant information, leading to reduced accuracies (Wang et al., 2022a).

At Ofunato station, the first tsunami signals lasted for approximately an hour until 22:30 UTC 21 November 2016. After the arrival of the first tsunami wave, ~30 min time lapses of quiescence were visible on the spectra, followed by another energetic period band that ranged between 9.1 and 22.5 min after 23:00 UTC 21 November 2016. Both first and second tsunami signals featured dominant tsunami period bands of 9.1–22.5 min. Sharing similar wave period range as with the first tsunami signals, the second tsunami signal appeared to be a reflected wave from Fukushima coast (Fig. 8). The second signals lasted for approximately 1 h and possessed a longer period of approximately 28.8 min afterwards. The period band of 28.8 min was of high energy and a longer duration (~3 h). Oscillation was generated in this period band approximately 3 h after the earthquake origin time, and 2 h after the arrival of the first tsunami signal at this station. Similar feature is also
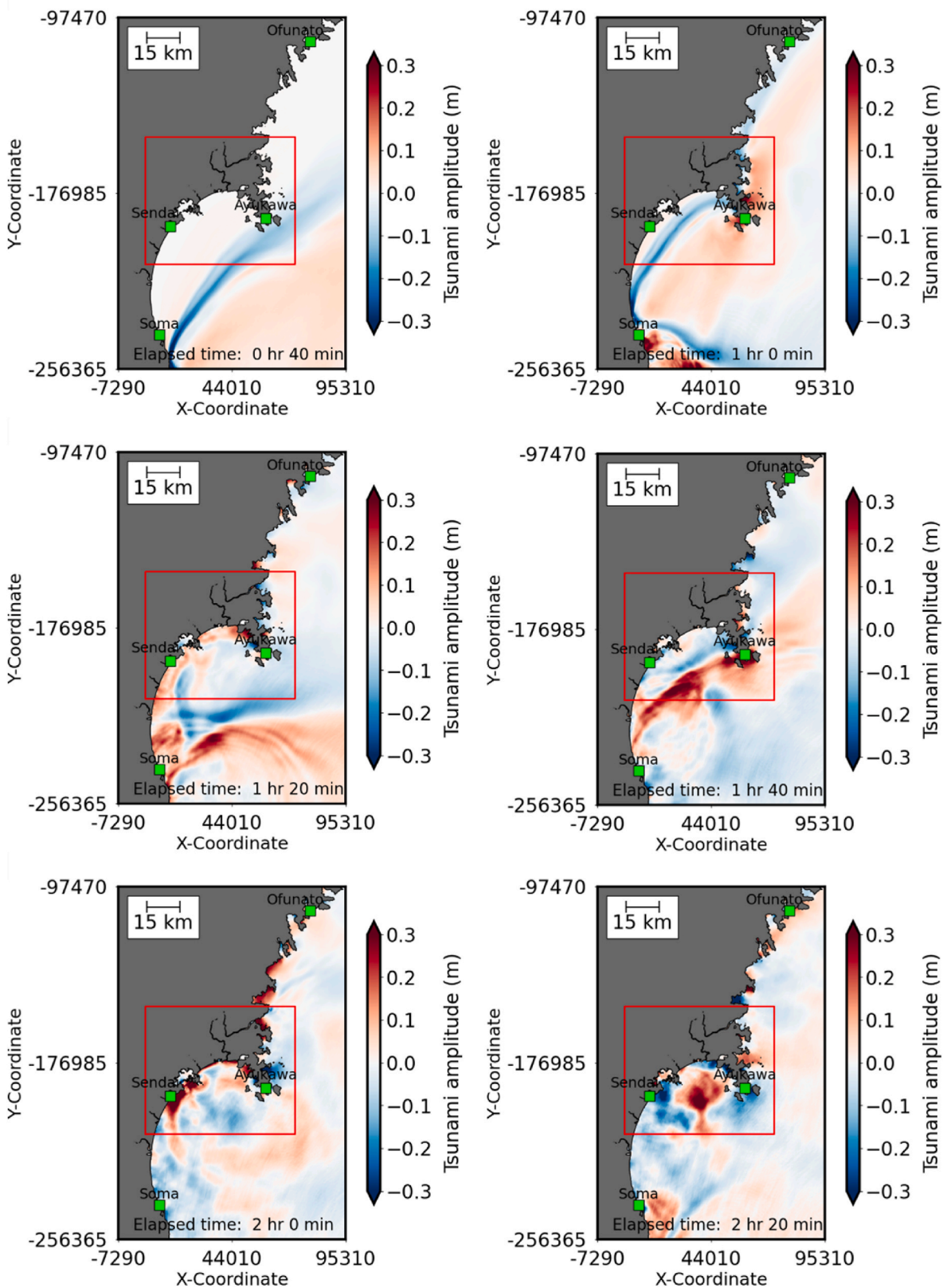
Fig. 9. Snapshots of simulated tsunami propagation along the Sendai Bay coast following the 2016 Fukushima earthquake. Red rectangles show the area where wave heights were significantly amplified within the Sendai Bay.
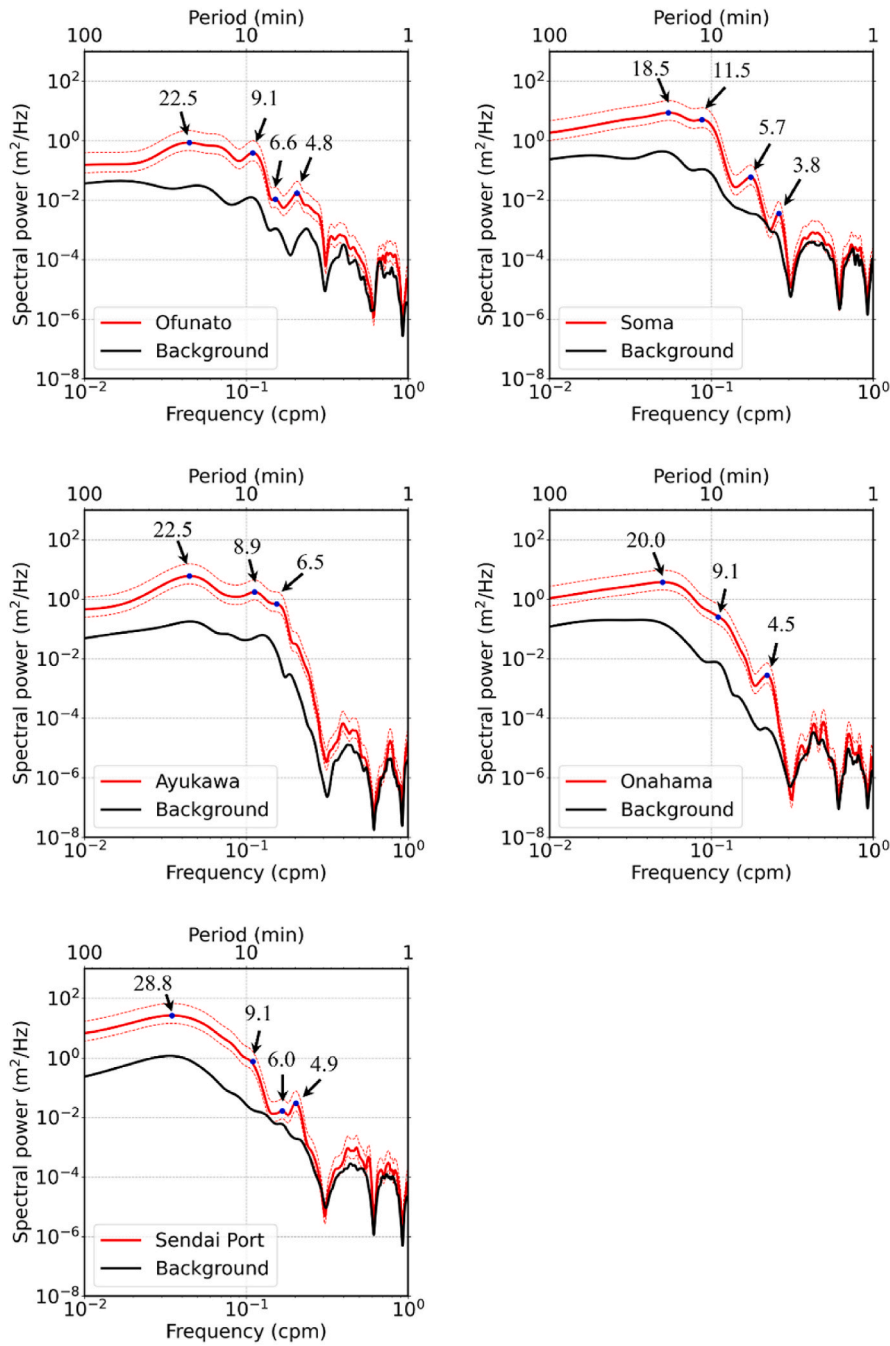
Fig. 10. Spectral analysis for tsunami records at coastal tide gauges. The solid red lines denote the tsunami spectra. The dashed red lines show the 95% confidence bounds of tsunami spectra. The solid black lines represent the background spectra. The peak periods are marked by blue points.

visible in wavelet spectra of Soma and Ayukawa stations.

The wavelet plot of Sendai Port reveals a long-lasting (∼3 h) wave at period of 9.1–22.5 min following the arrival of first tsunami signals at this station. This wave appeared to be affected by the reflections in Sendai Bay (Fig. 9) as it contained similar wave periods as the first tsunami signals. Approximately 4 h after the arrival time of the first tsunami signals, the energy level was diminished and mainly distributed at periods approximately 28.8–38.0 min. This period band possessed a remarkably long-lasting wave for more than 12 h which is not seen in other stations. Investigation on various triggered modes of the November 2016 tsunami event and their subsequent impacts to Sendai Bay region requires a separate analysis, which is presented in Section 3.5.

3.5. Tsunami resonance analysis

We conducted spatio-temporal spectral analysis to investigate the resonance characteristics and their oscillation patterns around the Sendai Bay during the November 2016 tsunami. The main tsunami oscillation periods were identified from the spatially integrated spectra of all calculated grids. The spatially integrated spectrum can be estimated by using the following equation (Catalán et al., 2015):

$$\widehat{S}(f) = \frac{\iint S(x, y, f) dx dy}{\iint dx dy} \tag{5}$$

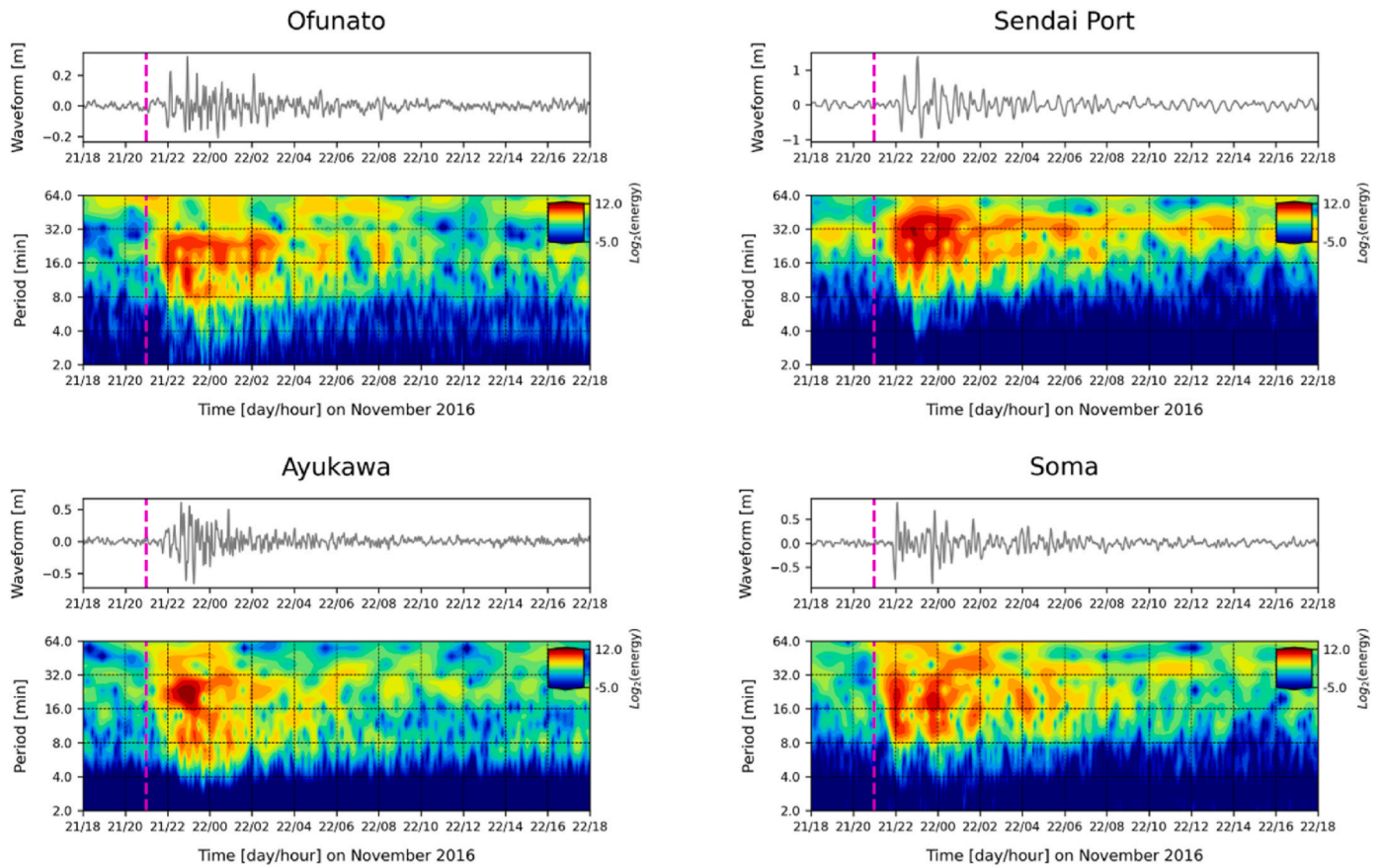where $S(x, y, f)$ is the spectrum calculated at each computational grid

Fig. 11. Wavelet plots for coastal tide data around Sendai Bay for the tide gauge records of the 2016 Fukushima tsunami. The magenta dashed lines indicate the earthquake occurrence time.

point of region 2, and $\widehat{S}(f)$ is the mean value of the spatially integrated spectra corresponding to frequency f. This approach has been previously applied by Wang et al. (2022b) and Cheng et al. (2023b) to obtain main tsunami oscillation periods. Based on the spatially integrated spectrum (Fig. 12), we identified six main tsunami oscillation periods for the 2016 tsunami event: 10 min, 12 min, 16 min, 24 min, 26 min, and 38 min. For each of these oscillation periods, Fourier analysis was applied to simulated time series for all computational grid points of region 2 to obtain the spatial distribution of phase and spectral amplitude (Figs. 13 and 14).

The tsunami oscillation at 38 min displays a high energy wave system, with well-defined nodes in Sendai Bay and extended offshore to the open boundary (Fig.. 13a and 14a). This period also excited significant energy amplification at regions around Oshika Peninsula. The oscillation period of 26 min reflected a similar wave structure as 38 min but with high-energy wave mainly concentrated around Sendai Bay and Oshika Peninsula (Fig.. 13b and 14b). This high-energy wave visibly weakened as it extended offshore from Sendai Bay to the open sea. The peak period at Sendai Port station identified in our Fourier analysis (i.e., 28.8 min) is consistent with this oscillation period (Fig. 10).
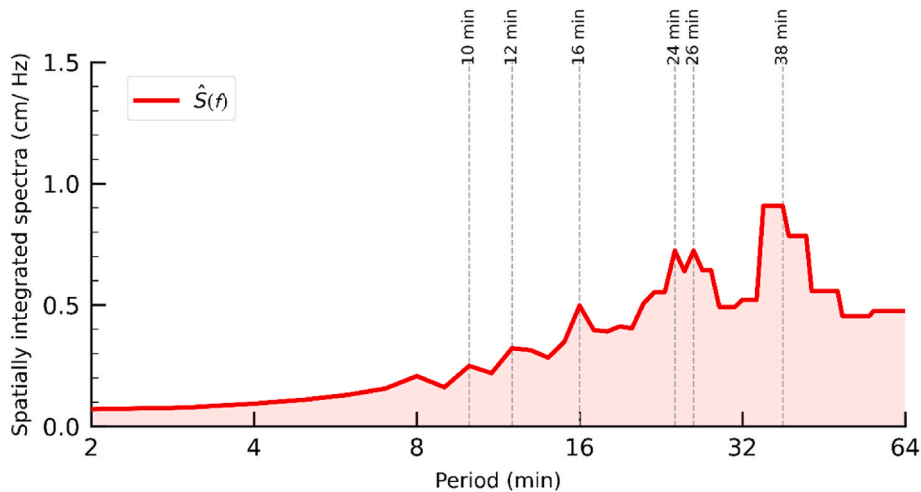

Fig. 12. Spatially integrated spectra (solid red line) and main tsunami oscillation periods (marked by gray dashed lines) of the 2016 Fukushima tsunami event.
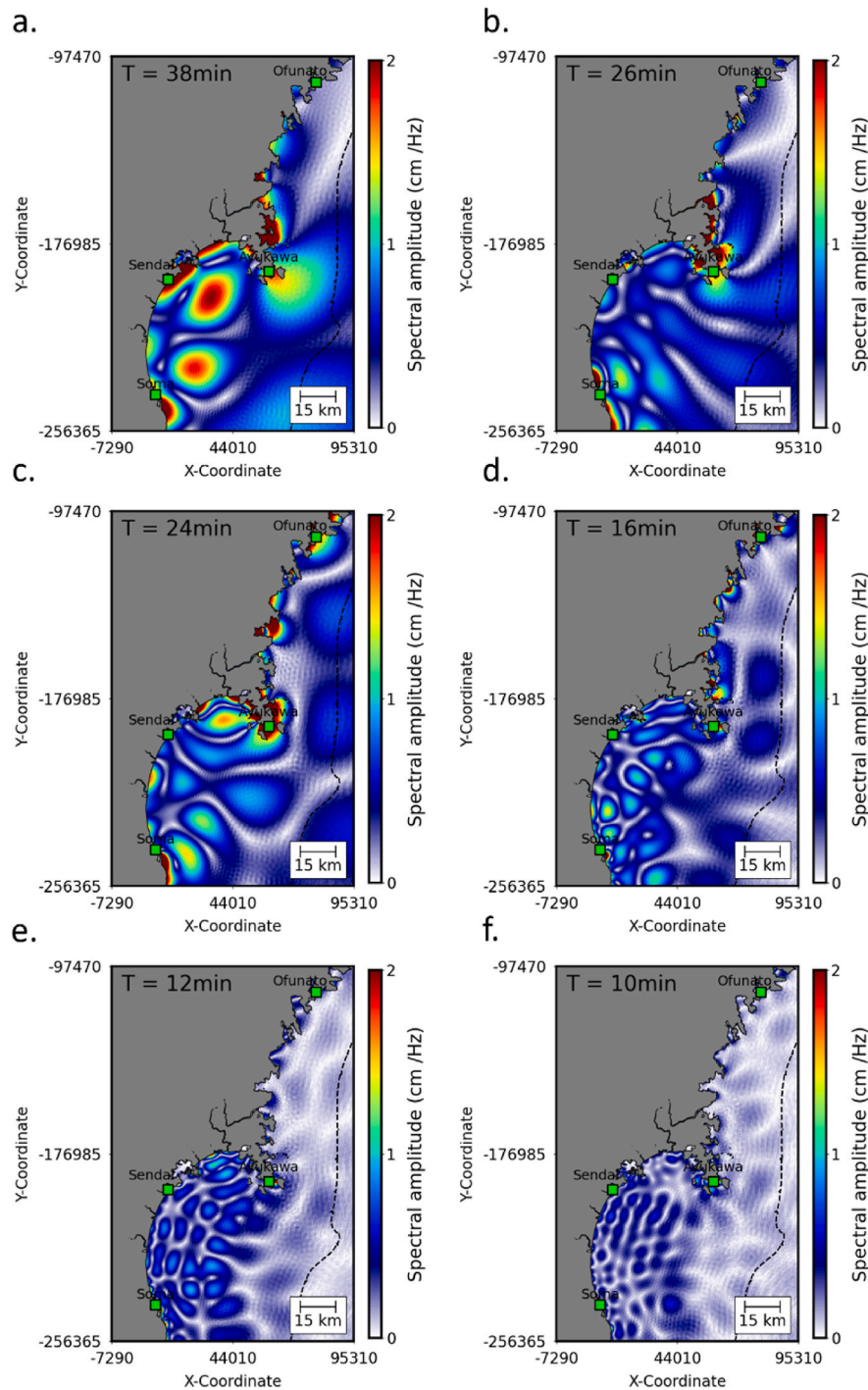
Fig. 13. Spatial distribution of the calculated spectral amplitudes of resonance periods around Sendai Bay during the 2016 Fukushima tsunami for various wave periods. The green squares represent coastal tide stations. The dashed lines are the sea depth contours of 200 m.

As the period decreases from 26 min to 24 min, the high energy wave system is shortened as new nodes appear in the Sendai Bay (Figs.. 13c and 14c). Similar to the wave oscillation at period of 26 min, the antinodes of 24 min also triggered high-energy wave in Sendai Bay and Oshika Peninsula but at a weaker energy level. This period matches the spectral peak of Ayukawa and Ofunato station at 22.5 min (Fig. 10). Energy amplification inside the Sendai Bay occurred at the antinodes at oscillation period of 16 min but at a lower energy level (Figs.. 13d and 14d). This period matches the spectral peaks at Soma station and Onahama station of 18.5 min and 20.0 min, respectively (Fig. 10). Similar to the

oscillations at period of 16 min, the oscillation at period of 12 min shows antinodes with high energy level appearing only inside the Sendai Bay (Figs.. 13e and 14e). This oscillation period is similar to dominant periods of 11.5 min at Soma station. Unlike other periods, the oscillation period at 10 min demonstrates relatively weak tsunami energy level inside the Sendai Bay (Figs.. 13f and 14f). This period corresponds to the energetic peak of 9.1 min at Ofunato, Sendai Port, and Onahama stations, and 8.9 min at Ayukawa station (Fig. 10). Besides, the phase angle changes slowly as wave period increases (Fig. 14). This is expected as the tsunami wavelength with a longer wavelength can be transported in a smoother
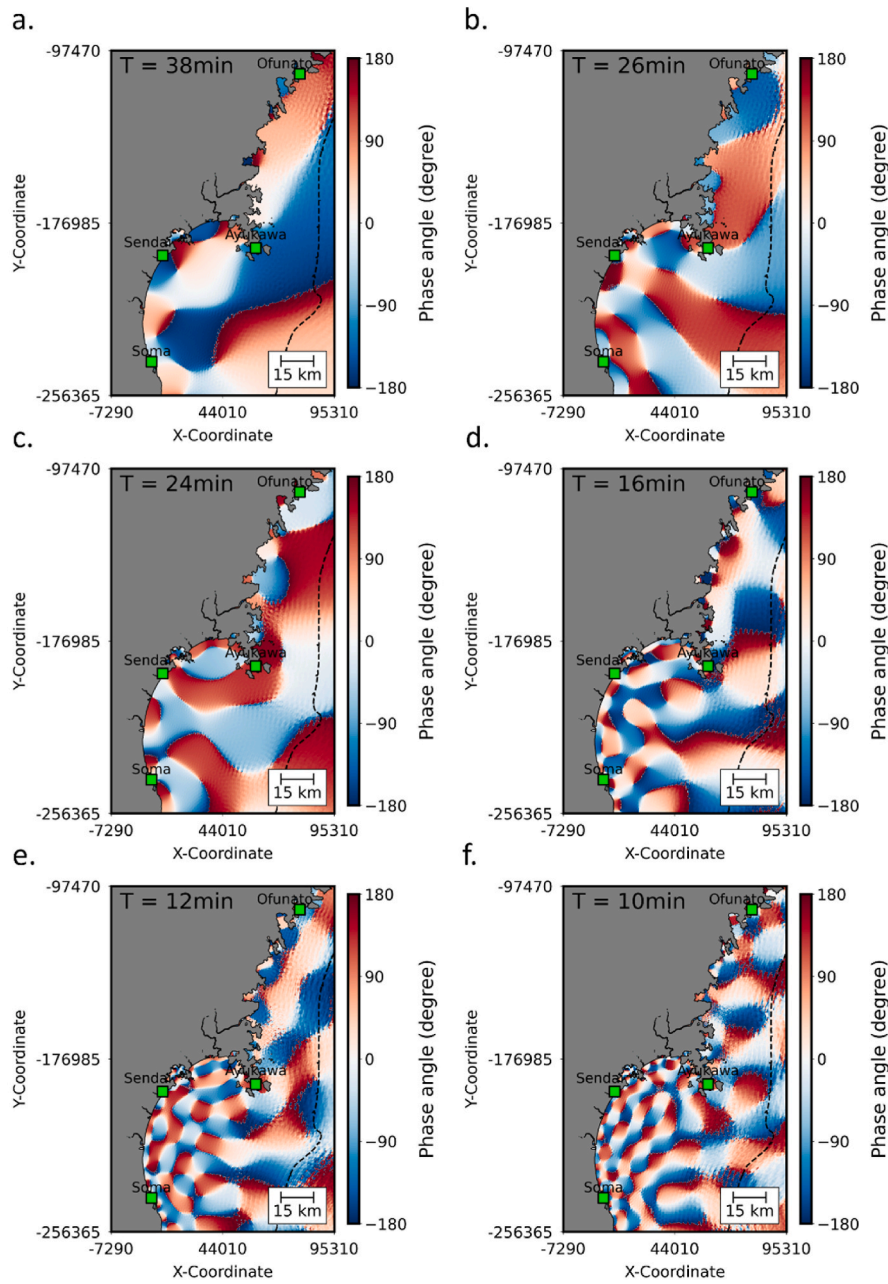
Fig. 14. Spatial distribution of the calculated phase angle of resonance periods around the Sendai Bay during the 2016 Fukushima tsunami for various periods. The green squares denote the coastal tide stations. The dashed lines are the sea depth contours of 200 m.

phase angle (Cheng et al., 2023b).

4. Discussion

The Mw 6.9 Fukushima earthquake on 21 November 2016, triggered a tsunami recorded by tide stations along north Pacific coast of Japan. The tsunami activity lasted for several hours, and at specific stations such as Sendai Port, Ayukawa, and Ofunto, the largest tsunami wave appeared in the later phase. Delayed arrival of largest waves and long-lasting tsunami oscillation has been previously attributed to the presence of edge waves (Munger and Cheung, 2008; Roeber et al., 2010; Koyano et al., 2021; Wang et al., 2022b; Cheng et al., 2023a), or the excitation of basin fundamental modes and coupling influence with edge waves (Yamazaki and Cheung, 2011; Catalán et al., 2015; Cortés et al., 2017; Melgar and Ruiz-Angulo, 2018).

To investigate the possible excitation of the resonance modes, we analyzed the tsunami dependency on the tsunami source and local bathymetric features. A way to estimate the nominal tsunami source periods is to look at the size of the co-seismic crustal deformation and applying the relationship proposed by Heidarzadeh and Satake (2015). The relationship can be expressed as follows.

$$T = \frac{2L}{\sqrt{gh}} \tag{6}$$

where L is the source characteristic length (i.e., width or length of the fault), h is the sea depth around the earthquake epicentral region, and g is the gravitational acceleration (9.81 m s^{-1}). Here, we used the validated source model of Adriano et al. (2018) where the size of the 2016 Fukushima earthquake is 40 km (long axis) $\times$ 32 km (short axis). The sea depth around the co-seismic deformation area is approximately

150–400 m (Fig. 5). By assuming a mean sea depth of 275 m around the deformation area, the nominal tsunami source periods originated from the width and length of the source are estimated at 20.5 min, and 25.7 min, respectively. We note that the tsunami period estimated from Equation (6) is a nominal one and does not account for the heterogeneity and complexity of the sources and the bathymetry; however, it is useful as it gives a rough estimate of the tsunami source period. Comparing this nominal tsunami period with the three period bands identified from Fourier analysis, it can be seen that the nominal source period (i.e., 20.5–25.7 min) matches well with the longest period band identified from Fourier spectra (i.e., 18.5–22.5 min).

Snapshots of simulated tsunami propagation reveals the patterns of tsunami wave alongshore of Fukushima and Miyagi Prefectures (Figs. 8 and 9). The snapshots demonstrate wave reflections and the presence of edge waves, with notable energy concentration at specific sites. To address this, we applied the relationship proposed by González et al. (1995). The relationship can be expressed as follows.

$$L_n = \frac{\alpha(2n+1)gT^2}{2\pi} \tag{7}$$

where, L is the wavelength of edge wave mode, α is the slope of seafloor, T is the period of fundamental modes of edge wave, g is the gravitational acceleration, and n is the various fundamental modes ($n = 0, 1, 2$). By assuming a seafloor slope of 0.0025 and a tsunami wavelength of ~10 km along coastline of Sendai Bay (see snapshots in Figs. 13 and 14), the fundamental period of mode-0 edge wave are estimated to be ~26.7 min, which is fairly consistent with the dominant wave periods of 28.8 min at Sendai Port station (Fig. 10). It is noteworthy that the simple model of equation (7) gives rough estimation of edge wave mode, however, it suggests that at least some of the dominant periods observed corresponding to the edge wave.

The long period oscillations (i.e., >28.8 min) appear to be more noticeable in areas where the shelf is wider, i.e., Sendai Bay. To test the possible excitation of Sendai Bay oscillation, we applied the relationship proposed by Rabinovich (2010). The relationship can be expressed as follows.

$$T_n = \frac{4L}{(2n+1)\sqrt{gh}} \tag{8}$$

where, T is the period of fundamental oscillation mode, L is the length of the rectangular semi-confined basin, h is the average sea depth of the basin, g is the gravitational acceleration, and n is the various fundamental modes. By assuming a bay length of 40 km and an average sea depth of 50 m in Sendai Bay (see Fig. 2), the fundamental oscillation periods ($n = 0, 1, 2$) are estimated to be 120.4 min, 40.1 min, and 24.0 min. The first fundamental oscillation mode of 40.1 min is consistent with the oscillation period of ~38 min, identified as one of the main oscillation periods of the 2016 Fukushima tsunami event (Fig. 12).

Finally, to provide further insights on the tsunami impacts due to the excitation of tsunami resonance inside the Sendai Bay, the peak spectral amplitude around the Sendai Bay is computed and plotted in Fig. 15a. Tsunami energy was mainly focused inside the Sendai Bay and the north coast of the Oshika Peninsula, consistent with the peak tsunami amplitude simulated using source model of Adriano et al. (2018) (Fig. 15b). This indicates that the energy amplifications of the 2016 Fukushima tsunami in the Sendai Bay and Oshika Peninsula are related to excitation of resonance modes.

5. Conclusions

Tsunami waveform analysis, spectral analysis, as well as tsunami simulation were employed to explore the tsunami wave characteristics at tide gauges and the mechanisms of large amplification of the 2016 Fukushima tsunami in the Sendai Bay. The main findings are summarized as follows.

1. The maximum crest amplitude was 0.32–1.38 m on the examined tide records, and the maximum tsunami amplitude occurred 8–56 min after the first tsunami arrivals. We attributed the late arrivals of the largest tsunami waves to phenomena such as wave reflections and edge waves, as well as oscillations inside the Sendai Bay.

2. The period band of the 2016 Fukushima tsunami was 3.8–22.5 min and the long oscillations in the Sendai Bay was due to the longer wave periods of approximately 28.8–38 min. We identified the
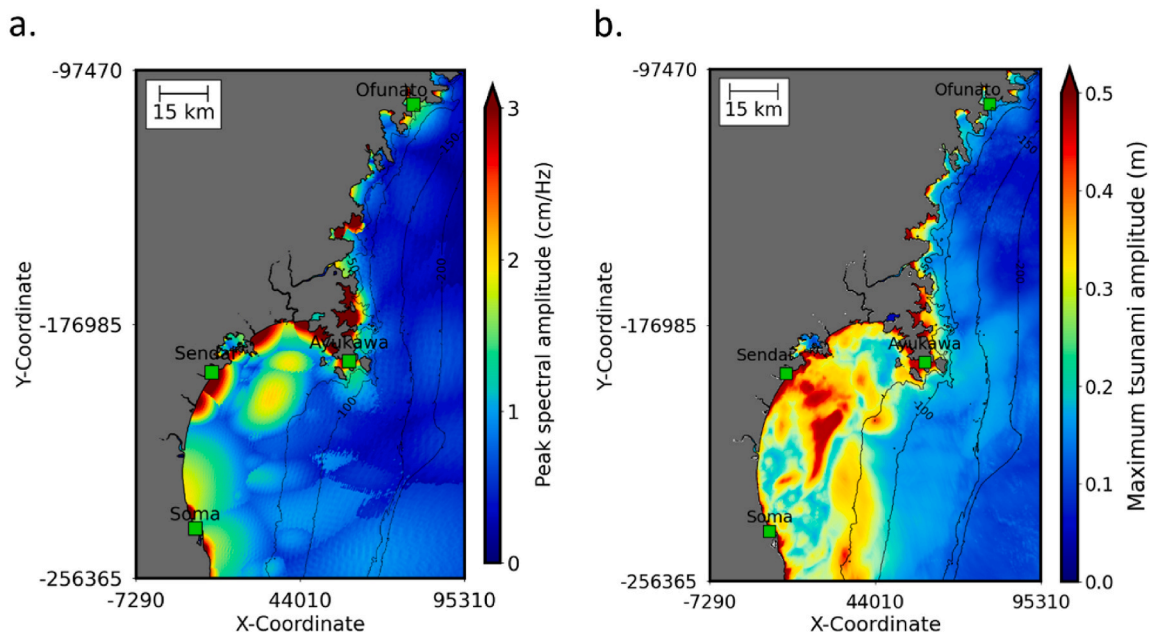

Fig. 15. Spatial distribution of the (a) peak spectral amplitude and (b) simulated maximum tsunami amplitude around the Sendai Bay and Oshika Peninsula during the 2016 Fukushima tsunami. The green triangles represent coastal tide gauges. The black lines are the sea depth contours at 50 m intervals.

period of 18.5–22.5 min as belonging to the tsunami source, whereas the dominant periods of longer than 28.8 min are attributed to non-source phenomena, such as shelf edge waves and oscillations of the Sendai Bay.

3. The spectral amplitude and phase angle distribution showed anti-nodes with energy amplification inside the Sendai Bay and Oshika Peninsula in most oscillation periods. The peak spectral amplitude distribution matches well with simulated wave heights around the Sendai Bay, indicating that the tsunami waves were entrapped along the coast and hence, result in resonance amplifications.

One of the key targets of the Sendai Framework for Disaster Risk Reduction (United Nations International Strategy for Disaster Reduction, 2015) by 2030 is to substantially reduce disaster damage to critical infrastructure and disruption to basic services. Although no substantial damage has been reported, the 2016 Fukushima tsunami offers important insights into tsunami behavior along the Fukushima coast and the potential for local amplification of the waves in the Sendai Bay during future tsunami events. As illustrated throughout this study, tsunami within bays can oscillate at their own natural frequencies even several hours after the arrival of the first wave, causing substantial damage to critical infrastructure along the coast. As the Sendai port is one of the major ports in the Tohoku region of Japan, such processes can have severe consequences on the port's operations (Chua et al., 2021). A better understanding and interpretations of tsunami waveform characteristics at tide stations can also aid in successful and timely issuance and cancellation of tsunami warnings.

CRediT authorship contribution statement

An-Chi Cheng: Conceptualization, Formal analysis, Writing – original draft. **Anawat Suppasri:** Supervision, Writing – original draft. **Mohammad Heidarzadeh:** Formal analysis, Writing – review & editing. **Bruno Adriano:** Writing – review & editing. **Constance Ting Chua:** Writing – original draft. **Fumihiko Imamura:** Supervision, Writing – review & editing.

Declaration of competing interest

The authors declare that they have no competing interests regarding the work presented in this paper.

Data availability

Data will be made available on request.

References

Adriano, B., Fujii, Y., Koshimura, S., 2018. Tsunami Source and Inundation Features Around Sendai Coast, Japan, Due to the November 22, 2016 M W 6.9 Fukushima Earthquake. Geosci Lett. https://doi.org/10.1186/s40562-017-0100-9.

Catalán, P.A., Aránguiz, R., González, G., Tomita, T., Cienfuegos, R., González, J., Shrivastava, M.N., Kumagai, K., Mokrani, C., Cortés, P., Gubler, A., 2015. The 1 april 2014 pisagua tsunami: observations and modeling. Geophys. Res. Lett. 42, 2918–2925. https://doi.org/10.1002/2015GL063333.

Cheng, A.-C., Suppasri, A., Pakoksung, K., Imamura, F., 2023a. Characteristics of consecutive tsunamis and resulting tsunami behaviors in southern Taiwan induced by the Hengchun earthquake doublet on 26 December 2006. Nat. Hazards Earth Syst. Sci. 23, 447–479. https://doi.org/10.5194/nhess-23-447-2023.

Cheng, A.-C., Suppasri, A., Pakoksung, K., Imamura, F., 2023b. Resonance characteristics and impact of the 2006 Pingtung tsunami in southern Taiwan. Geosci Lett 10, 17. https://doi.org/10.1186/s40562-023-00271-0.

Cortés, P., Catalán, P.A., Aránguiz, R., Bellotti, G., 2017. Tsunami and shelf resonance on the northern Chile coast. J Geophys Res Oceans 122, 7364–7379. https://doi.org/10.1002/2017JC012922.

Chua, C.-T., Switzer, A., Suppasri, A., Li, L., Pakoksung, K., Lallemant, D., Jenkins, S.F., Charvet, I., Chua, T., Cheong, A., Winspear, N., 2021. Tsunami Damage to Ports: Cataloguing Damage to Create Fragility Functions from the 2011 Tohoku Event, Natural Hazards and Earth System Sciences 21 1887–1908. https://doi.org/10.5194/nhess-21-1887-2021, 2021.

Goto, C., Ogawa, Y., Shuto, N., Imamura, F., 1997. Numerical Method of Tsunami Simulation with the Leap-Frog Scheme.

Gusman, A.R., Satake, K., Shinohara, M., Sakai, S., Tanioka, Y., 2017. Fault slip distribution of the 2016 Fukushima earthquake estimated from tsunami waveforms. Pure Appl. Geophys. 174, 2925–2943. https://doi.org/10.1007/s00024-017-1590-2.

González, F.I., Satake, K., Boss, E.F., Mofjeld, H.O., 1995. Edgewave and non-trapped modes of the 25 april 1992 cape mendocinotsunami. Pure Appl. Geophys. 144 (3–4), 409–426. https://doi.org/10.1007/BF00874375.

Hayashi, Y., 2021. Sensitivity of tsunami height distribution to fault model parameters: case study based on the 2016 off fukushima earthquake. Journal of JSCE, B2 (Coastal Engineering) 77. I_187-I_192.

Heidarzadeh, M., Satake, K., Murotani, S., Gusman, A.R., Watada, S., 2015. Deep-water characteristics of the trans-pacific tsunami from the 1 april 2014 M w 8.2 iquique, Chile earthquake. Pure Appl. Geophys. 172, 719–730. https://doi.org/10.1007/s00024-014-0983-8.

Heidarzadeh, M., Satake, K., 2015. New insights into the source of the Makran tsunami of the 27 November 1945 from tsunami waveforms and coastal deformation data. Pure Appl. Geophys. 172 (3), 621–640.

Heidarzadeh, M., Necmioglu, O., Ishibe, T., Yalciner, A.C., 2017. Bodrum–Kos (Turkey–Greece) Mw 6.6 Earthquake and Tsunami of 20 July 2017: a Test for the Mediterranean Tsunami Warning System. Geosci Lett. https://doi.org/10.1186/s40562-017-0097-0.

Heidarzadeh, M., Ishibe, T., Sandanbata, O., Muhari, A., Wijanarto, A.B., 2020. Numerical modeling of the subaerial landslide source of the 22 December 2018 Anak Krakatoa volcanic tsunami, Indonesia. Ocean Eng. 195, 106733 https://doi.org/10.1016/j.oceaneng.2019.106733.

Heidarzadeh, M., Gusman, A.R., 2021. Source modeling and spectral analysis of the crete tsunami of 2nd may 2020 along the hellenic subduction zone, offshore Greece. Earth Planets Space 73. https://doi.org/10.1186/s40623-021-01394-4.

Heidarzadeh, M., Mulia, I.E., 2021. Ultra-long period and small-amplitude tsunami generated following the July 2020 Alaska Mw7.8 tsunamigenic earthquake. Ocean Eng. 234 https://doi.org/10.1016/j.oceaneng.2021.109243.

Heidarzadeh, M., Pranantyo, I.R., Okuwaki, R., Dogan, G.G., Yalciner, A.C., 2021. Long tsunami oscillations following the 30 october 2020 Mw 7.0 aegean sea earthquake: observations and modelling. Pure Appl. Geophys. 178, 1531–1548. https://doi.org/10.1007/s00024-021-02761-8.

Heidarzadeh, M., Gusman, A.R., Ishibe, T., Sabeti, R., Šepić, J., 2022. Estimating the eruption-induced water displacement source of the 15 January 2022 Tonga volcanic tsunami from tsunami spectra and numerical modelling. Ocean Eng. 261 https://doi.org/10.1016/j.oceaneng.2022.112165.

Heidarzadeh, M., Mulia, I.E., 2022b. A new dual earthquake and submarine landslide source model for the 28 September 2018 Palu (Sulawesi), Indonesia tsunami. Coast Eng. J. 1–13. https://doi.org/10.1080/21664250.2022.2122293.

Imamura, F., 1996. Review of tsunami simulation with a finite difference method. Long-wave Run-up Models 25–42.

Japan Meteorological Agency (JMA), 2016. Press releases (in Japanese). http://www.jma.go.jp/jma/press/1611/22b/kaisetsu201611221100.pdf. (Accessed 14 January 2023).

Japan Society of Civil Engineers (JSCE), 2016. Tsunami Assessment Method for Nuclear Power Plants in Japan. Available at: https://committees.jsce.or.jp/ceofnp/system/files/TAM2016_main_202010.pdf. (Accessed 31 July 2023).

Kuramoto, K., Suppasri, A., Imamura, F., 2018. Summarizing of the lessons from the 2016 fukushima earthquake and tsunami assessment using database. Journal of JSCE, B2 (Coastal Engineering) 74. I_535-I_540.

Koyano, K., Takabatake, T., Esteban, M., Shibayama, T., 2021. Influence of edge waves on tsunami characteristics along kujukuri beach, Japan. J. Waterw. Port, Coast. Ocean Eng. 147, 04020049, 10. 1061/(ASCE) WW. 1943- 5460. 00006 17.

Munger, S., Cheung, K.F., 2008. Resonance in Hawaii waters from the 2006 kuril islands tsunami. Geophys. Res. Lett. 35 (7), L07605 https://doi.org/10.1029/2007GL032843.

Melgar, D., Ruiz-Angulo, A., 2018. Long-lived tsunami edge waves and shelf resonance from the M8.2 tehuantepec earthquake. Geophys. Res. Lett. 45 (12) https://doi.org/10.1029/2018GL080823, 414–12,421.

Okada, Y., 1985. SURFACE DEFORMATION DUE TO SHEAR AND TENSILE FAULTS IN A HALF-SPACE. Carolrhoda Books.

Rabinovich, A.B., 1997. Spectral analysis of tsunami waves: separation of source and topography effects. J Geophys Res Oceans 102, 12663–12676. https://doi.org/10.1029/97JC00479.

Rabinovich, A.B., 2010. Seiches and harbor oscillations. In: Handbook of Coastal and Ocean Engineering, pp. 193–236.

Roeber, V., Yamazaki, Y., Cheung, K.F., 2010. Resonance and impact of the 2009 Samoa tsunami around tutuila, American Samoa. Geophys. Res. Lett. 37 (21), L21604 https://doi.org/10.1029/2010GL044419.

Suppasri, A., Leelawat, N., Latcharote, P., Roeber, V., Yamashita, K., Hayashi, A., Ohira, H., Fukui, K., Hisamatsu, A., Nguyen, D., Imamura, F., 2017. The 2016 Fukushima earthquake and tsunami: local tsunami behavior and recommendations for tsunami disaster risk reduction. Int. J. Disaster Risk Reduc. 21, 323–330. https://doi.org/10.1016/j.ijdrr.2016.12.016.

Suppasri, A., Nishida, T., Pakokung, K., Cheng, A.-C., Chua, C.-T., Iwasaki, T., Pescaroli, G., Imamura, F., 2022. Quantifying tsunami impact on industrial facilities and production capacity in ports: an application to Sendai Port, Japan. Int. J. Disaster Risk Reduc. 78 (2022), 103141 https://doi.org/10.1016/j.ijdrr.2022.103141.

Tanioka, Y., Satake, K., 1996. Tsunami generation by horizontal displacement of ocean bottom. Geophys. Res. Lett. 23, 861–864. https://doi.org/10.1029/96GL00736.

Torrence, C., Compo, G.P., 1998. Apractical guide to wavelet analysis. Bull. Am. Meteorol. Soc. 79 (1), 61–78.

United States Geological Survey (Usgs), 2016. M6.9–37 Km ESE of Namie, Japan. http://earthquake.usgs.gov/earthquakes/eventpage/us10007b88#executive. (Accessed 14 January 2023).

United Nations International Strategy for Disaster Reduction (UNISDR), 2015. Sendai Framework for Disaster Risk Reduction 2015–2030. UNISDR, Geneva. https://www.undrr.org/publication/sendai-framework-disaster-risk-reduction-2015-2030. (Accessed 10 May 2023).

Wang, Y., Zamora, N., Quiroz, M., Satake, K., Cienfuegos, R., 2021. Tsunami resonance characterization in Japan due to trans-pacific sources: response on the bay and continental shelf. J Geophys Res Oceans 126. https://doi.org/10.1029/2020JC017037.

Wang, Y., Heidarzadeh, M., Satake, K., Hu, G., 2022a. Characteristics of two tsunamis generated by successive Mw 7.4 and Mw 8.1 earthquakes in the kermadec islands on 4 March 2021. Nat. Hazards Earth Syst. Sci. 22, 1073–1082. https://doi.org/10.5194/nhess-22-1073-2022.

Wang, Y., Su, H.Y., Ren, Z., Ma, Y., 2022b. Source properties and resonance characteristics of the tsunami generated by the 2021 M 8.2 Alaska earthquake. J Geophys Res Oceans 127. https://doi.org/10.1029/2021JC018308.

Yamazaki, Y., Cheung, K.F., 2011. Shelf resonance and impact of near-field tsunami generated by the 2010 Chile earthquake. Geophys. Res. Lett. 38 (12), L12605, 10.1029/2011G L0475 08.